Using GISAXS to detect correlations between the locations of gold particles electrodeposited from aqueous solution

Gilles E. Moehl, Philip N. Bartlett, and Andrew L. Hector*

School of Chemistry, University of Southampton, Southampton SO17 1BJ, UK

* E-mail: A.L:Hector@soton.ac.uk

Abstract

Electrodeposition is a powerful tool for the bottom up fabrication of novel electronic devices. This necessitates complete understanding of the deposition process beyond the classical description using current transients. Recent calculations predict deviations within the spatial arrangement of electrodeposited particles, away from random nucleation. The spatial arrangement of Au particles generated through aqueous electrodeposition on a non-templated substrate is investigated by Grazing Incidence Small Angle X-ray Scattering (GISAXS). We show that GISAXS is able to reveal spatial correlations within deposited particles which are not easily detectable by microscopy.

Introduction

In the field of catalysis and optoelectronics, an appreciation of the importance of the size-dependent properties of gold nanoparticles has increased over recent years.[1–4] Gold nanoparticles can be produced in colloidal form in a variety of shapes using self-assembling surfactants.[5]

Electrodeposition is an effective way to modify a surface by forming nanoparticles, where the size and number density of the nuclei depend on the chosen experimental parameters. The technique requires a deep understanding of its mechanisms when applied within nanostructured templates, where deposition needs to homogeneously occur at smallest distances on comparatively large surfaces. On these small length scales, the influence of (nanoscale) local physicochemical effects as e.g. the depletion of electrochemically available species in the vicinity of a single deposited nucleus have to be taken into consideration. This requires the investigation of the overall particle arrangement for specific electrochemical conditions.

The study of nucleation in electrodeposition has a long history with significant advances being made in the 1950s.[6] Much of the fundamental description of electrochemical nucleation was established in the 1980s and 1990s,[7–13] nevertheless there still remain areas of disagreement

and continued development.[14,15] Scharifker and Mostany were the first to report a general theoretical description of the current transients obtained during three-dimensional electrochemical nucleation on a finite number of active sites, taking into account the overlap of growth centers during diffusion limited growth[8]. This model was refined by Sluyters and Rehbach,[9] then by Heerman and Tarrallo.[10] The essential element within the theoretical considerations is the concept of planar diffusion zones and their overlap, using so-called nucleation exclusion zones around the nuclei. Scharifker et al. later described the spatial distribution of nucleation rates around growing spherical nuclei in which zones of reduced nucleation are the result of calculating the realistic rate distribution around nuclei.[7,8] Their explanation includes the broadening of size distributions from overlapping diffusion fields, which were then demonstrated experimentally by Liu et al. by using conditions of decoupled growth in order to achieve narrower size distributions.[12,13,16,17] Additionally, they show through simulations that the nearest neighbour distances for the 1st, 2nd and 3rd neighbours differ from random nucleation. For Pb, Ag and Cu this was later shown experimentally by using electron microscopy, where the nearest neighbour distance follows a geometrical progression.[18,19] From a theoretical viewpoint, this mechanism was recently described analytically by Tomellini, and elucidates how the nearest neighbour distribution of particles evolves from Poissonian to non-random pair correlations during progressive nucleation.[20] These models assume that nuclei/nanoparticles are immobile on the surface after nucleation, although this is challenged by the work of Ustarroz et al. who imaged individual nuclei during electrodeposition using transmission electron microscopy.[15] Most recently, Mamme et al. presented numerical calculations of nanocluster diffusion and aggregative growth, showing the importance of including the surface mobility of clusters into the theoretical considerations around electrochemical nucleation.[21]

Grazing incidence small angle X-ray scattering (GISAXS) is a surface sensitive technique that has been used in the past mainly to investigate soft matter systems.[22–25] GISAXS allows for the analysis of surfaces in the range of mm^2, many times larger than the areas studied by electron microscopy (typically of the order of 10-50 μm^2). Thus GISAXS could give improved statistics on the underlying morphological and structural arrangement of the electrodeposited particles, especially for detecting any sort of order. GISAXS has been used recently for the *in situ* investigation of sputter deposition on different inorganic and organic substrates, and for spray deposition of various materials, where the formation of the deposited materials was followed in real time.[22–24,26–30] For electrochemical systems, only a handful of studies using X-rays (both transmission SAXS, GISAXS and surface XRD) can be found in the literature. Ustarroz et al. looked at the deposition of silver nanoparticles on carbon using SAXS.[31,32] Golks et al. examined the dissolution of a gold (100) surface in a chloride containing solution[33] and Magnussen et al. reported the surface dynamics of gold deposited on a gold (100) surface.[34,35] In this work, we have used GISAXS to investigate the electrodeposition of gold from an aqueous solution on TiN, a widely used material in microelectronics and an increasingly popular electrode material.[36] The study of Au electrodeposition has been mainly addressed in the past using glassy carbon or n-Si electrodes,[19,37–39] We show that even though electron microscopy is very useful as a characterization method for these systems, the use of GISAXS allows for the detection of non-random order within a seemingly disordered arrangement of particles, proving that nucleation during electrodeposition of Au on TiN is not a fully random process.

Experimental Section

A sketch of the experimental setup used for these experiments and the geometry of the GISAXS experiments are given in the supplementary information **(Figure S1)**. A TiN coated Si working electrode (150 mm^2), a Pt counter electrode and a Ag/AgCl reference electrode (saturated KCl)

were assembled in a typical three-electrode electrochemical cell setup. The surface of the working electrode was confined to 10 × 15 mm. The blank Si substrates (no pre-treatment) were coated with 200 nm of TiN by magnetron sputtering (Buehler Helios, rate: 0.135 nm/s), which results in surfaces with a roughness of 1 nm (H=0.349, lateral correlationlength=20.72 nm. Our measurements are consistent with data from Kirchner et al.[36]). The electrolyte consisted of 0.001 mol dm^{-3} $K[AuCl_4]$ with 0.1 mol dm^{-3} KCl (supporting electrolyte) in deionized water. The electrolyte was purged with N_2 for 15 min prior to every experiment to remove dissolved oxygen. Before and after deposition, each sample was rinsed using deionized water. Both reagents were purchased from Sigma Aldrich and used as received. SEM images of each sample were taken on the same day at which deposition was done. GISAXS experiments were carried out at beamline 7.3.3 SAXSWAXS of the Advanced Light Source in Berkeley, California (Shipping time 1 day (Fedex), measurement done 4 weeks after deposition). Acquisitions were for 1 s per image at an incident angle α_i of 0.567°, beam energy of 10 keV and sample to detector distance of 3529 mm (Dectris Pilatus 2M, pixelsize: (172 x 172) μm^2). The incoming X-ray beam (300 µm (H) x 700 µm (W)) impinges on the sample surface under the angle α_i with the wavevector k_i, and exits with a wavevector k_f. The momentum transfer q is the difference in magnitude between incoming and outgoing ($q = k_f - k_i$) waves, which relates to the wavevector given by

$$q_{x,y,z} = \frac{2\pi}{\lambda} \begin{pmatrix} \cos(\alpha_f)\cos(\varphi) - \cos(\alpha_i) \\ \cos(\alpha_f)\sin(\varphi) \\ \sin(\alpha_i) + \sin(\alpha_f) \end{pmatrix} \quad (1)$$

in Cartesian coordinates. The q values in reciprocal space correspond to real-space distances via $d = \frac{2\pi}{q}$.[40] For any GISAXS image the occurrence of an intensity maximum (Yoneda peak) is typical at $q_y = 0$ and a q_z value which depends on the material and substrate.[41] When

integrating the intensity profiles in q_y (horizontal cut) at the position of this characteristic peak in q_z, structural information can be obtained.[42]

Results and Discussion

The electrochemical system was characterized using cyclic voltammetry at a scan rate of 50 mV s^{-1} starting from open circuit potential (0.7 V vs. Ag/AgCl) to -1.0 V, then to 1.2 V and back, as shown in **Figure 1a)**. The reduction peak at 0.2 V during the first cathodic scan can be attributed to the initial deposition of gold on the TiN substrate. In aqueous chloride solutions containing $[AuCl_4]^-$ there are three possible anodic redox couples with the reactions:[37,43–45]

$$AuCl_4^- + 3e^- \rightarrow Au + 4Cl^- \; E_0 = 802 \text{ mV vs.} \frac{Ag}{AgCl} \quad (2)$$

$$AuCl_4^- + 2e^- \rightarrow AuCl_2^- + 2Cl^- \; E_0 = 726 \text{ mV vs.} \frac{Ag}{AgCl} \quad (3)$$

$$AuCl_2^- + e^- \rightarrow Au + 2Cl^- \; E_0 = 951 \text{ mV vs.} \frac{Ag}{AgCl} \quad (4)$$

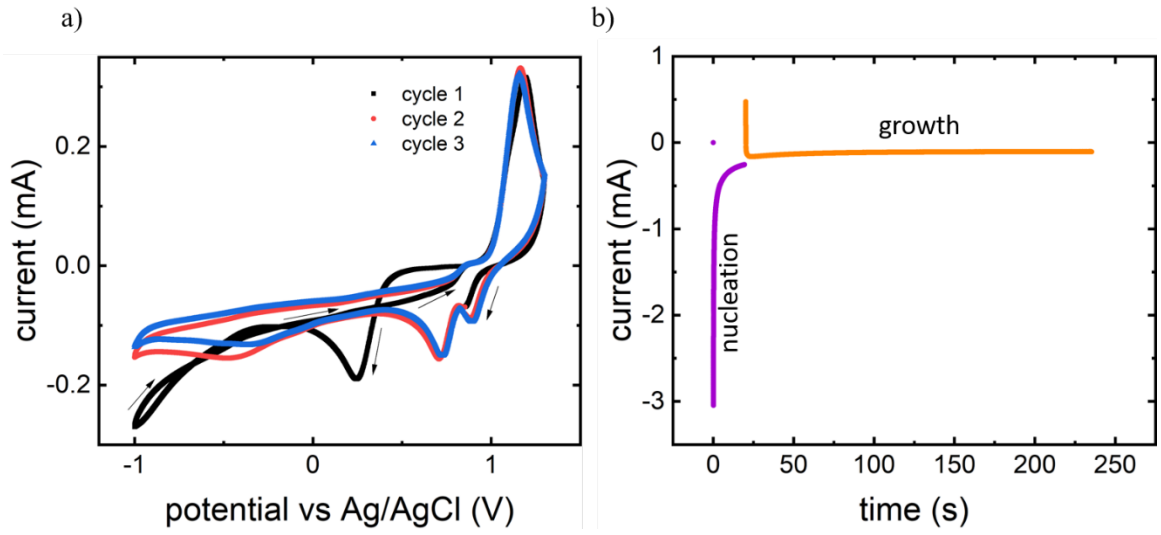

Figure 1: a) Cyclic voltammetry of the aqueous gold deposition electrolyte (1 mM K[$AuCl_4$] with 0.1 M KCl) with a scan rate of 50 mV s^{-1} using TiN working (15 mm^2), Pt mesh counter and Ag/AgCl reference (saturated KCl) electrodes. b) Current transients of deposition at a nucleation potential of -1 V and growth potential of 0 V.

A nucleation loop is observed below -0.5 V in this first scan. In subsequent scans, the gold reduction peak shifts to more positive potentials, which indicates that the deposition of Au on Au is favored versus TiN. The transition from just one to two reduction peaks in scans 2 and 3 indicates the presence of both Au(III) and Au(I) complexes and both species can be reduced to Au(0) during deposition. The corresponding oxidation (stripping) peak is seen just above 1.0 V which also agrees with previous work on this system.[37] **Figure 1b)** shows the current transients obtained during deposition of Au using a high nucleation overpotential at -1.0 V for 0.056 mC mm^{-2} followed by growth at 0 V until reaching a total surface charge density of 0.222 mC mm^{-2}. Depositions were carried out with fixed charge densities using -1.0 V and -2.0 V as nucleation potentials (0.056 mC mm^{-2}) and 0, -0.4 and -0.8 V as growth potentials respectively (0.222 mC mm^{-2}). Every sample was then analyzed by scanning electron microscopy (SEM); images are shown in **Figure 2a)** for nucleation at -1 V and **Figure 2b)** at -2 V. From these SEM images, the radii of the particles were extracted using ImageJ[46] and plotted in Figure **S2 a), b)**. Distributions of the corresponding the particle radii are shown in **Figure S5**. One can see that for higher nucleation overpotential, (more –ve potential) or shorter growth periods, the particle size distributions migrate towards smaller values. This corresponds to expectations, as the critical size a nucleus needs to exceed for successful nucleation decreases with greater driving force (overpotential).[6]

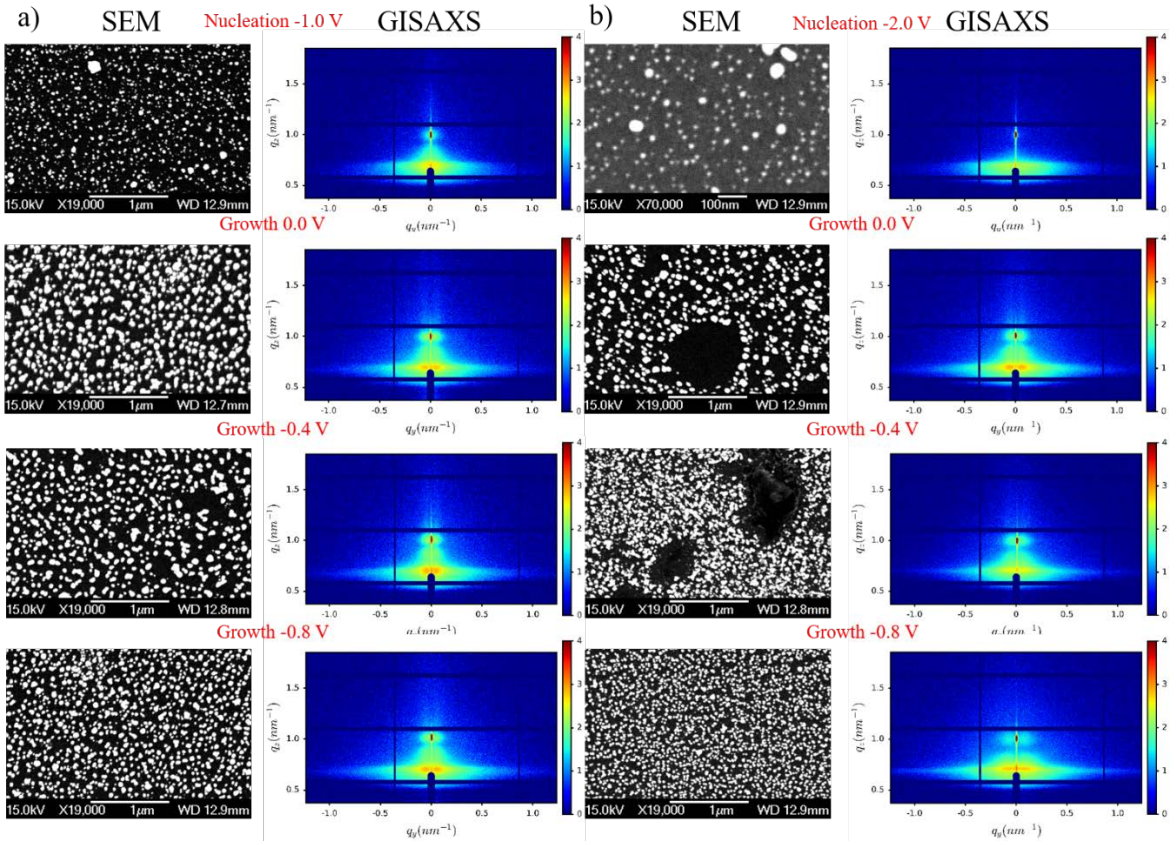

Figure 2: SEM (left) and GISAXS (right) images of particles formed after a nucleation pulse at a) -1.0 V and b) -2.0 V with consecutive growth steps at either 0.0, -0.4 or -0.8 V.

In order to reveal the spatial arrangement of the Au particles, GISAXS experiments were carried out. The two-dimensional detector images are shown in **Figure 2** next to their corresponding SEM data. One can observe the occasional occurrence of deposition-less areas in the SEM images, which we attribute to pre-deposition contamination. Due to their micron scale size, these areas are not visible in the GISAXS data, as they are outside the detectable range of length scales of the experiment. Horizontal line profiles were extracted from the raw data using the DPDAK[47] software package by projecting the intensity at the Yoneda position onto the q_y axis; these which are shown in **Figure 3a)** for -1.0 V and -2.0 V nucleation potentials respectively. The profiles show a broad peak for both potentials, where the lower potential peak has a higher q value, which means that the correlation distance d (see inset **Figure 3a**)) for the particles deposited at higher nucleation overpotential (-2.0 V) is shorter

than that for the particles deposited at lower nucleation overpotential. The same procedure was applied to the images taken after the respective growth periods, in **Figure 3b)** and **Figure 3c)**. The values for the correlation distances do not strongly depend on the growth potential but rather on the nucleation potential. For -1.0 V nucleation, distances around 120 nm are observed, while for -2.0 V nucleation potential, the *d* values are smaller (average below 100 nm). The GISAXS correlation distances (*d*) are contrasted with the nearest neighbor distance extracted from SEM data (*nnd)* in the insets of **Figure 3 b)** and **c).** The distances obtained from the GISAXS data are significantly larger in all cases. Generally, using a larger nucleation overpotential results in a smaller distance between particles as more particles nucleate.[6]

In order to understand why the correlation distances obtained from GISAXS (*d*) are larger than the apparent nearest neighbor distance (*nnd)*, the SEM images from **Figure 2 a)** were revisited. The larger correlation lengths indicate the possibility that not all particles present contribute to the correlation distance observed in the GISAXS data, but rather that the contributing particles possess a higher degree of ordering than the whole distribution. To verify this, subsets of the particle distribution were analyzed for their nearest neighbor distance and particle density. The threshold for the smallest particles to be included into the *nnd** calculations was increased from zero to the largest value at which particles were still counted. This means that particles were filtered out from the bottom end of the radial distribution. For each increment, *nnd**, the reduced number density, *N**, of the particles was evaluated. The corresponding graphs are shown in the Supporting Information **Figure S3** a) for -1 V nucleation and b) -2 V nucleation potential. When increasing the lower particle radius threshold, the nearest neighbor distance *nnd** at first increases slowly but then diverges rapidly for the higher values. From these graphs the lower particle radius threshold corresponding to the *nnd** value equal to the distance obtained from GISAXS, is extracted. In turn this yields a value for the number of particles which are placed at that distance to each other. If the particles were randomly distributed on

the substrate, their distance *d* could be calculated from their number density *N* by $d_{\mathrm{uni}} = \frac{1}{2} N^{-\frac{1}{2}}$. For a square array, the distance would be $d_{\mathrm{sq}} = N^{-\frac{1}{2}}$ and for hexagonally packed particles $d_{\mathrm{hex}} = 1.0746\, N^{-\frac{1}{2}}$.[19] This means that the resulting number densities can be compared to the ones calculated from the *d* values to show which arrangement fits best. The number density N_{sq} and N_{uni}, calculated from the correlation distance obtained in GISAXS as well as the reduced number density N^*, calculated from the number of particles remaining after filtering out smaller particles as explained above are summarized in **Figure 4a)** and **b)** for -1 V and -2V nucleation potential respectively. It can be seen that the reduced number density N^* consistently takes a value higher than would be expected for disordered particles, which indicates that this particular part of the distribution is not randomly distributed, but possesses some ordering. This effect can also be evaluated by looking at the nearest neighbor index $I_{NN} = nnd/d_{uni}$, which indicates ordering of dispersed particles for values greater than 1 and particle clustering for values lower than 1. A corresponding plot for particles deposited at -1 V nucleation and 0 V growth can be seen in **Figure 4c)**. It shows a maximum of I_{NN} when increasing the lower particle threshold, followed by a rapid decay of the curve to values below 1. The increasing values at the beginning of the curve indicate that the larger particles are better ordered than the smaller ones, while the decay towards the largest particle sizes indicates that these are not actual spherical particles of that size, but clusters that were falsely identified during data treatment. This explains why the nearest neighbor distance from the microscopy does not quite fit to the GISAXS data, as the increased ordering of the larger particles leads to a stronger scattering signal. To further investigate our assumptions, simulations of the system within the Distorted Wave Born Approximation (DWBA) were done using the dedicated software BornAgain[48]. As parameters, values from the previously analyzed SEM and GISAXS data were used in a model consisting of a spherical formfactor and a radial paracrystal as the

interference function. The results from these simulations are compared to the raw data in **Figure S4**, showing that our assumptions fit the raw data reasonably well. Further details on the simulations can be found in the SI. For additional comparison, GISAXS data of a blank TiN substrate are shown in **Figure S6** (measured on our in house instrument (Rigaku Smartlab).

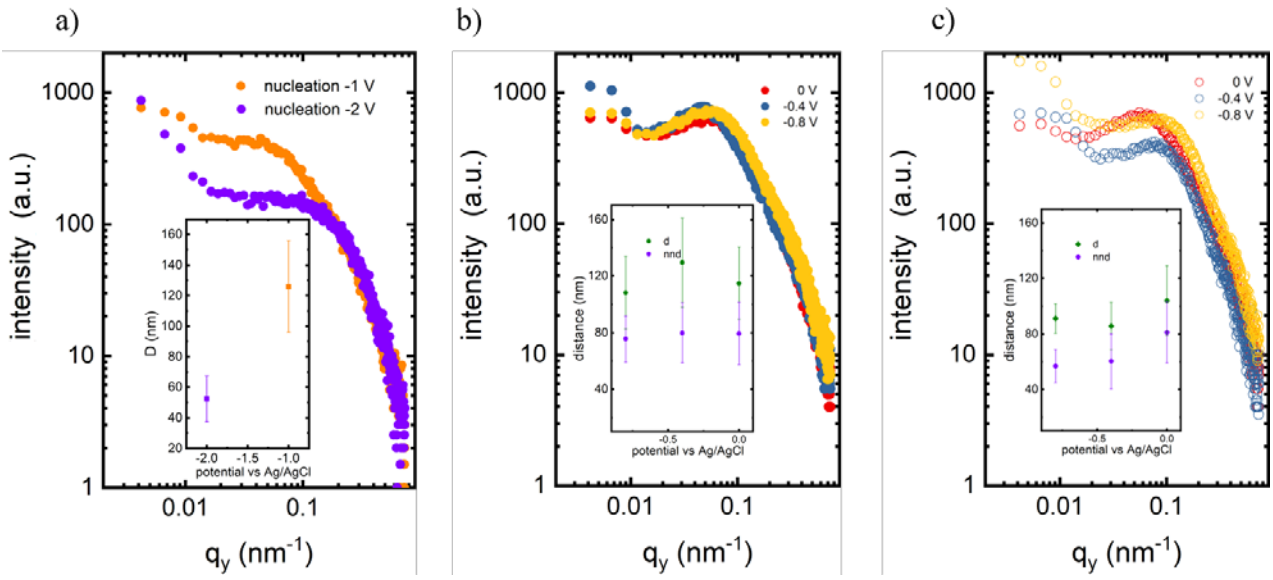

Figure 3: a) Horizontal cuts of GISAXS data from particles nucleated at -1.0 V and -2.0 V respectively. Inset: correlation distances *d* extracted from curves in a). b) Horizontal GISAXS profiles of particles deposited at -1.0 V nucleation potentials and 0, -0.4, -0.8 V respectively. Inset: *d*, and *nnd* corresponding to data in (a). c) Horizontal GISAXS profiles of particles deposited at -2.0 V nucleation potentials and 0, -0.4, -0.8 V respectively. Inset: *d*, and *nnd* corresponding to data in (c).

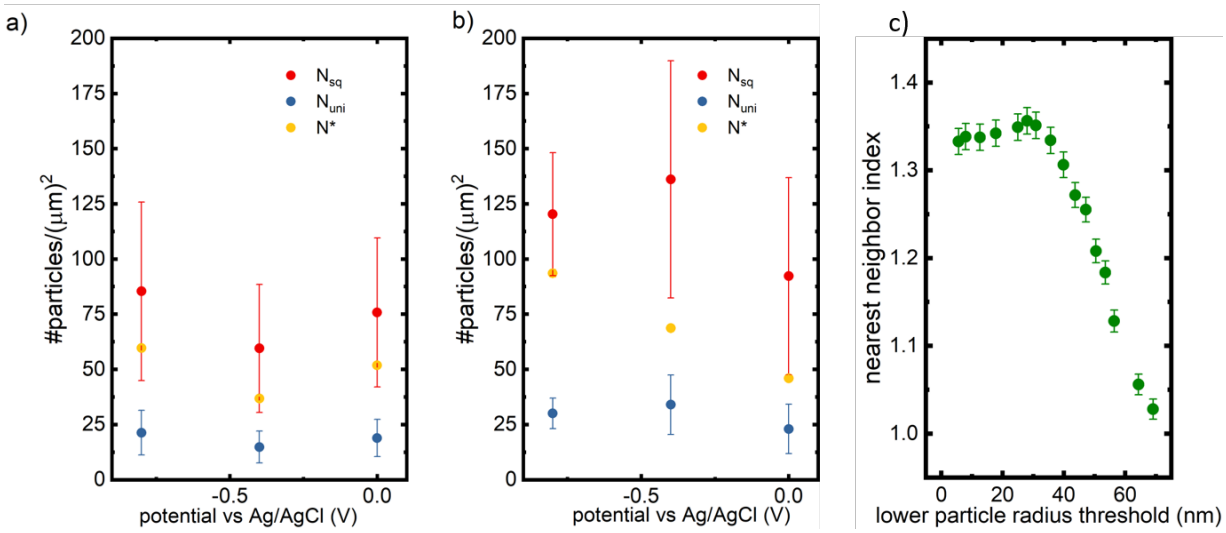

Figure 4: The number density N_{sq} and N_{uni}, calculated from the correlation distance obtained in GISAXS as well as the reduced number density N* calculated from the particles remaining in the distribution with a value of nnd* corresponding to d are plotted in a) for -1.0 V and b) -2.0 V nucleation. c) Nearest neighbor index $I_{NN} = nnd/d_{uni}$ of particles deposited at -1 V nucleation and 0 V growth for different values of the lower particle size threshold.

The first step in the experiment was the application of a high overpotential nucleation pulse leading to rapid initial deposition of small nuclei due to the high nucleation rate. This is expected from theoretical predictions[49] and confirmed by electron microscopy (see **Figure 2**). With a diffusion coefficient of $D \cong 10^{-5}cm^2/s$,[50] the diffusion layer $\delta=\sqrt{\pi}Dt$ expands beyond 100 nm in less than 5 microseconds. The fast overlap of diffusion zones quickly enlarges the areas of reduced nucleation and thus modulates the favored surface for nucleation, meaning that zones of enhanced and reduced nucleation alternate across the electrode surface. As a consequence, during nucleation particles do not randomly distribute on the surface but nucleate with similar distances to each other as the ones corresponding to a square/hexagonal array (close packed), and their distance depends on the nucleation rate (higher rate, smaller distances). Following this, the remaining space is filled with particles in a less ordered manner during the growth period. The consecutive change of potential when going from the high nucleation overpotential to the lower growth overpotential reduces the nucleation rate and thus the current magnitude significantly, depending on the choice of growth potential (see **Figure**

1 b)). From our experiment, we know that within the error bars, the mean correlation distance detected in the GISAXS data does not differ significantly for the respective growth potentials 0 V, -0.4 V and 0.8 V. At the same time, the mean particle radii decrease with decreasing growth potential, which shows that through lowering the nucleation rate the growth of particles is increasingly favored. This in turn means that in the "growth" phase, particles generated during the nucleation pulse are more likely to expand in size at the expense of further nucleation, leading to the formation of two size regimes. This explains why a longer distance than the nearest neighbor distance is obtained from the GISAXS data, since the technique probes the film on a very large scale in which the larger particles seem to be dominating the scattering pattern because they have a higher degree of ordering.

Summary and Conclusions

In this work we have shown that GISAXS is a valuable technique to reveal structural properties of nanoparticle films that cannot be directly detected by microscopy. In the present case GISAXS demonstrates the presence of zones with reduced nucleation, which would not only need enormous amounts of measurement time to be observed by electron microscopy but also a large amount of computing power to reveal information with similar quality. The combined use of electron microscopy and scattering enables the elucidation of nucleation mechanisms that are otherwise difficult to observe. For the electrodeposition of gold on TiN using GISAXS we have shown that the spatial arrangement of electrodeposited gold nanoparticles has a non-random distribution. The surface itself should not impose any geometrical constraints on the process since the surface is not patterned and extremely flat (roughness of 1 nm)), even though it has been shown that TiN made by PVD grows in a columnar fashion[51] (with much smaller dimensions than the structures observed in this work). This kind of insight is especially significant for the use of nanostructured electrodes, as it indicates possible limitations of the electrodeposition when using, for example, a nanoporous template on top of an electrode,

where the packing could be so dense that the pore distance is of similar distance to the diffusion layers around each pore.[52] In such a case, a non-homogeneous filling of the template would occur if pores happen to reside in a zone of reduced nucleation, i.e. the ones around a pore that had already been successfully filled. Simulations of nanoelectrode arrays have shown that with increasing pore density and decreasing aspect ratio, the nanoelectrode array behaves more and more like a non-structured electrode of equivalent surface area.[53,54] This does of course not take into account the actual diffusion process inside the nanopores, which will differ strongly from classical models, especially when the dimensions approach the size of the electrochemical species. Future investigations of electrodeposition into porous templates will be needed in order to properly understand the process.

Acknowledgements

This work has been supported by EPSRC through the Advanced Devices by Electroplating program grant (ADEPT; EP/N035437/1). The GISAXS data was collected during the GISAS summer school 2018 (Bayreuth) using beamline 7.3.3 of the Advanced Light Source which is supported by the Director of the Office of Science, Office of Basic Energy Sciences, of the U.S. Department of Energy under Contract No. DE-AC02-05CH11231. PNB acknowledges receipt of a Royal Society Wolfson Research Merit-Award. The authors would like to thank Dr. Ruomeng Huang for providing the required roughness data of the TiN substrates.

Supporting Information

Electrochemical setup and conditions, average particle sizes, nearest neighbor distances, DWBA simulation details and results, particle radii distributions, blank TiN substrate GISAXS data

References

(1) Daniel, M. C. M.; Astruc, D. Gold Nanoparticles: Assembly, Supramolecular Chemistry, Quantum-Size Related Properties and Applications toward Biology, Catalysis and Nanotechnology. *Chem. Rev.* **2004**, *104*, 293–346.

(2) Ghosh, P.; Han, G.; De, M.; Kim, C. K.; Rotello, V. M. Gold Nanoparticles in Delivery Applications. *Adv. Drug Deliv. Rev.* **2008**, *60* (11), 1307–1315.

(3) Eustis, S.; El-Sayed, M. A. Why Gold Nanoparticles Are More Precious than Pretty Gold: Noble Metal Surface Plasmon Resonance and Its Enhancement of the Radiative and Nonradiative Properties of Nanocrystals of Different Shapes. *Chem. Soc. Rev.* **2006**, *35* (3), 209–217.

(4) Kreuzer, L. P.; Männel, M. J.; Schubert, J.; Höller, R. P. M.; Chanana, M. Enzymatic Catalysis at Nanoscale: Enzyme-Coated Nanoparticles as Colloidal Biocatalysts for Polymerization Reactions. *ACS Omega* **2017**, *2* (10), 7305–7312.

(5) Li, N.; Zhao, P.; Astruc, D. Anisotropic Gold Nanoparticles: Synthesis, Properties, Applications, and Toxicity. *Angew. Chemie - Int. Ed.* **2014**, *53* (7), 1756–1789.

(6) Holze, R. E. Budevski, G. Staikov, W. J. Lorenz Electrochemical Phase Formation and Growth. *Berichte der Bunsengesellschaft für Phys. Chemie* **2012**, *101* (7), 1081–1081.

(7) Scharifker, B.; Hills, G. Theoretical and Experimental Studies of Multiple Nucleation. *Electrochem. Acta* **1983**, *28* (7), 879–889.

(8) Scharifker, B.; Mostany, J. Three-Dimensional Nucleation with Diffusion Controlled Growth. *J.Electroanal.Chem.* **1984**, *177*, 13–23.

(9) Sluyters-Rehbach, M.; Wijenberg, J. H. O. J.; Bosco, E.; Sluyters, J. H. The Theory of Chronoamperometry for the Investigation of Electrocrystallization. Mathematical Description and Analysis in the Case of Diffusion-Controlled Growth. *J. Electroanal. Chem.* **1987**, *236* (1–2), 1–20.

(10) Heerman, L.; Tarallo, A. Theory of the Chronoamperometric Transient for Electrochemical Nucleation with Diffusion-Controlled Growth. *J. Electroanal. Chem.* **1999**, *470* (1), 70–76.

(11) Heerman, L.; Tarallo, A. Electrochemical Nucleation on Microelectrodes. Theory and Experiment for Diffusion-Controlled Growth. *J. Electroanal. Chem.* **1998**, *451* (1–2), 101–109.

(12) Liu, H.; Favier, F.; Ng, K.; Zach, M. P.; Penner, R. M. Size-Selective Electrodeposition of Meso-Scale Metal Particles: A General Method. *Electrochim. Acta* **2001**, *47* (5), 671–677.

(13) Liu, H.; Penner, R. M. Size-Selective Electrodeposition of Mesoscale Metal Particles in the Uncoupled Limit. *J. Phys. Chem. B* **2000**, *104* (39), 9131–9139.

(14) Hussein, H. E. M.; Maurer, R. J.; Amari, H.; Peters, J. J. P.; Meng, L.; Beanland, R.; Newton, M. E.; Macpherson, J. V. Tracking Metal Electrodeposition Dynamics from Nucleation and Growth of a Single Atom to a Crystalline Nanoparticle. *ACS Nano* **2018**,

12 (7), 7388–7396.

(15) Ustarroz, J.; Hammons, J. A.; Altantzis, T.; Hubin, A.; Bals, S.; Terryn, H. A Generalized Electrochemical Aggregative Growth Mechanism. *J. Am. Chem. Soc.* **2013**, *135* (31), 11550–11561.

(16) Milchev, A.; Kruijt, W. S.; Sluyters-Rehbach, M.; Sluyters, J. H. Distribution of the Nucleation Rate in the Vicinity of a Growing Spherical Cluster. Part 1. Theory and Simulation Results. *J. Electroanal. Chem.* **1993**, *362* (1–2), 21–31.

(17) Kruijt, W. S.; Sluyters, J. H.; Milchev, A. Distribution of the Nucleation Rate in the Vicinity of a Growing Spherical Cluster. *J. Electroanal. Chem.* **1994**, *371*, 13–26.

(18) Arzhanova, T.; Golikov, A. Long-Range Order in the Spatial Distribution of Electrodeposited Copper and Silver Nuclei on Glassy Carbon. *J. Electroanal. Chem.* **2003**, *558* (1–2), 109–117.

(19) Serruya, A.; Mostany, J.; Scharifker, B. R. Spatial Distributions and Saturation Number Densities of Lead Nuclei Deposited on Vitreous Carbon Electrodes. *J. Chem. Soc. Faraday Trans.* **1993**, *89* (2), 255–261.

(20) Tomellini, M. Spatial Distribution of Nuclei in Progressive Nucleation: Modeling and Application. *Phys. A Stat. Mech. its Appl.* **2018**, *496*, 481–494.

(21) Mamme, M. H.; Köhn, C.; Deconinck, J.; Ustarroz, J. Numerical Insights into the Early Stages of Nanoscale Electrodeposition: Nanocluster Surface Diffusion and Aggregative Growth. *Nanoscale* **2018**, *10* (15), 7194–7209.

(22) Kaune, G.; Ruderer, M. A.; Metwalli, E.; Wang, W.; Couet, S.; Schlage, K.; Röhlsberger, R.; Roth, S. V.; Müller-Buschbaum, P. In Situ GISAXS Study of Gold Film Growth on Conducting Polymer Films. *ACS Appl. Mater. Interfaces* **2009**, *1* (2), 353–360.

(23) Song, L.; Wang, W.; Körstgens, V.; Moseguí González, D.; Löhrer, F. C.; Schaffer, C. J.; Schlipf, J.; Peters, K.; Bein, T.; Fattakhova-Rohlfing, D.; In Situ Study of Spray Deposited Titania Photoanodes for Scalable Fabrication of Solid-State Dye-Sensitized Solar Cells. *Nano Energy* **2017**, *40*, 317–326.

(24) Song, L.; Wang, W.; Körstgens, V.; Moseguí González, D.; Yao, Y.; Minar, N. K.; Feckl, J. M.; Peters, K.; Bein, T.; Fattakhova-Rohlfing, D.; Spray Deposition of Titania Films with Incorporated Crystalline Nanoparticles for All-Solid-State Dye-Sensitized Solar Cells Using P3HT. *Adv. Funct. Mater.* **2016**, *26* (10), 1498–1506.

(25) Metwalli, E.; Nie, M.; Körstgens, V.; Perlich, J.; Roth, S. V.; Müller-Buschbaum, P. Morphology of Lithium-Containing Diblock Copolymer Thin Films. *Macromol. Chem. Phys.* **2011**, *212* (16), 1742–1750.

(26) Schwartzkopf, M.; Buffet, A.; Körstgens, V.; Metwalli, E.; Schlage, K.; Benecke, G.; Perlich, J.; Rawolle, M.; Rothkirch, A.; Heidmann, B.; From Atoms to Layers: In Situ Gold Cluster Growth Kinetics during Sputter Deposition. *Nanoscale* **2013**, *5* (11), 5053.

(27) Al-Hussein, M.; Schindler, M.; Ruderer, M. A.; Perlich, J.; Schwartzkopf, M.; Herzog, G.; Heidmann, B.; Buffet, A.; Roth, S. V.; Müller-Buschbaum, P. In Situ X-Ray Study of the Structural Evolution of Gold Nano-Domains by Spray Deposition on Thin

Conductive P3HT Films. *Langmuir* **2013**, *29* (8), 2490–2497.

(28) Schwartzkopf, M.; Santoro, G.; Brett, C. J.; Rothkirch, A.; Polonskyi, O.; Hinz, A.; Metwalli, E.; Yao, Y.; Strunskus, T.; Faupel, F.; Real-Time Monitoring of Morphology and Optical Properties during Sputter Deposition for Tailoring Metal − Polymer Interfaces. *ACS Appl. Mater. Interfaces* **2015**, *7*, 13547–13556.

(29) Schwartzkopf, M.; Hinz, A.; Polonskyi, O.; Strunskus, T.; Lo, F. C.; Ko, V.; Mu, P.; Faupel, F.; Roth, S. V. Role of Sputter Deposition Rate in Tailoring Nanogranular Gold Structures on Polymer Surfaces. *ACS Appl. Mater. Interfaces* **2017**, No. 9, 5629–5637.

(30) Santoro, G.; Yu, S.; Schwartzkopf, M.; Zhang, P.; Koyiloth Vayalil, S.; Risch, J. F. H.; Rübhausen, M. A.; Hernández, M.; Domingo, C.; Roth, S. V. Silver Substrates for Surface Enhanced Raman Scattering: Correlation between Nanostructure and Raman Scattering Enhancement. *Appl. Phys. Lett.* **2014**, *104* (24), 243107.

(31) Ustarroz, J.; Hammons, J. A.; Van Ingelgem, Y.; Tzedaki, M.; Hubin, A.; Terryn, H. Multipulse Electrodeposition of Ag Nanoparticles on HOPG Monitored by In-Situ by Small-Angle X-Ray Scattering. *Electrochem. commun.* **2011**, *13* (12), 1320–1323.

(32) Richardson, S. J.; Burton, M. R.; Luo, X.; Staniec, P. A.; Nandhakumar, I. S.; Terrill, N. J.; Elliott, J. M.; Squires, A. M. Watching Mesoporous Metal Films Grow during Templated Electrodeposition with: In Situ SAXS. *Nanoscale* **2017**, *9* (29), 10227–10232.

(33) Golks, F.; Krug, K.; Gründer, Y.; Zegenhagen, J.; Stettner, J.; Magnussen, O. M. High-Speed in Situ Surface X-Ray Diffraction Studies of the Electrochemical Dissolution of Au(001). *J. Am. Chem. Soc.* **2011**, *133* (11), 3772–3775.

(34) Magnussen, O. M.; Krug, K.; Ayyad, A. H.; Stettner, J. In Situ Diffraction Studies of Electrode Surface Structure during Gold Electrodeposition. *Electrochim. Acta* **2008**, *53* (9), 3449–3458.

(35) Ruge, M.; Golks, F.; Zegenhagen, J.; Magnussen, O. M.; Stettner, J. In Operando GISAXS Studies of Mound Coarsening in Electrochemical Homoepitaxy. *Phys. Rev. Lett.* **2014**, *112* (5), 1–5.

(36) Kirchner, C. N.; Hallmeier, K. H.; Szargan, R.; Raschke, T.; Radehaus, C.; Wittstock, G. Evaluation of Thin Film Titanium Nitride Electrodes for Electroanalytical Applications. *Electroanalysis* **2007**, *19* (10), 1023–1031.

(37) Komsiyska, L.; Staikov, G. Electrocrystallization of Au Nanoparticles on Glassy Carbon from HClO4solution Containing [AuCl4]-. *Electrochim. Acta* **2008**, *54* (2), 168–172.

(38) Milchev, A. Electrochemical Phase Formation on a Foreign Substrate—Basic Theoretical Concepts and Some Experimental Results. *Contemp. Phys.* **2007**, *32* (5), 321–332.

(39) Oskam, G.; Long, J. G.; Natarajan, A.; Searson, P. C. Electrochemical Deposition of Metals onto Silicon. *J. Phys. D. Appl. Phys.* **1998**, *31* (16), 1927–1949.

(40) Renaud, G.; Lazzari, R.; Leroy, F. Probing Surface and Interface Morphology with Grazing Incidence Small Angle X-Ray Scattering. *Surf. Sci. Rep.* **2009**, *64* (8), 255–380.

(41) Yoneda, Y. Anomalous Surface Reflection of X Rays. *Phys. Rev.* **1963**, *131* (5), 2010–2013.

(42) Lazzari, Â. Research Papers IsGISAXS : A Program for Grazing-Incidence Small-Angle X-Ray Scattering Analysis of Supported Islands Research Papers. *Interfaces (Providence).* **2002**, 406–421.

(43) Dudin, P. V; Unwin, P. R.; Macpherson, J. V. Electrochemical Nucleation and Growth of Gold Nanoparticles on Single-Walled Carbon Nanotubes: New Mechanistic Insights. *J. Phys. Chem. C* **2010**, *114* (i), 13241–13248.

(44) Goolsby, A. D.; Sawyer, D. T. Electrochemistry of Gold (I) and Its Complexes in Acetonitrile. *Anal. Chem.* **1968**, *40* (10), 1978–1983.

(45) Anderson, J. E.; Sawtelle, S. M. In Situ Generation and Characterization of Gold(I) Complexes from Potassium Tetrachloroaurate in Aqueous Solutions. *Inorg. Chim. Acta* **1992**, *194* (2), 171–177.

(46) Abràmoff, M. D.; Magalhães, P. J.; Ram, S. J. Image Processing with ImageJ. *Biophotonics Int.* **2004**, *11* (7), 36–41.

(47) Benecke, G.; Wagermaier, W.; Li, C.; Schwartzkopf, M.; Flucke, G.; Hoerth, R.; Zizak, I.; Burghammer, M.; Metwalli, E.; Müller-Buschbaum, P.; A Customizable Software for Fast Reduction and Analysis of Large X-Ray Scattering Data Sets: Applications of the New DPDAK Package to Small-Angle X-Ray Scattering and Grazing-Incidence Small-Angle X-Ray Scattering. *J. Appl. Crystallogr.* **2014**, *47* (5), 1797–1803.

(48) Burle, J., Durniak, C., Fisher, J.M., Ganeva, M., Pospelov, G., Van Herck, W., Wuttke, J., Yurov, D. BornAgain - Software for Simulating and Fitting X-Ray and Neutron Small-Angle Scattering at Grazing Incidence, Version 1.16. 2018.

(49) Bockris, J. O. *Electrochemical Phase Formation and Growth VCH*; VCH Verlagsgesellschaft, Weinheim, 2003; Vol. 433.

(50) Martín, H.; Carro, P.; Hernández Creus, A.; González, S.; Salvarezza, R. C.; Arvia, A. J. Growth Mode Transition Involving a Potential-Dependent Isotropic to Anisotropic Surface Atom Diffusion Change. Gold Electrodeposition on HOPG Followed by STM. *Langmuir* **1997**, *13* (1), 100–110.

(51) Robertson, C.; Beanland, R.; Boden, S. A.; Hector, A. L.; Kashtiban, R. J.; Sloan, J.; Smith, D. C.; Walcarius, A. Ordered Mesoporous Silica Films with Pores Oriented Perpendicular to a Titanium Nitride Substrate. *Phys. Chem. Chem. Phys.* **2015**, *17* (6), 4763–4770.

(52) Bartlett, P. N.; Beanland, R.; Burt, J.; Hasan, M. M.; Hector, A. L.; Kashtiban, R. J.; Levason, W.; Lodge, A. W.; Marks, S.; Naik, J.; Exploration of the Smallest Diameter Tin Nanowires Achievable with Electrodeposition: Sub 7 Nm Sn Nanowires Produced by Electrodeposition from a Supercritical Fluid. *Nano Lett.* **2018**, *18* (2), 941–947.

(53) Godino, N.; Borrise, X.; Muñoz, F. X.; Del Campo, F. J.; Compton, R. G. Mass Transport to Nanoelectrode Arrays and Limitations of the Diffusion Domain Approach: Theory and Experiment. *J. Phys. Chem. C* **2009**, *113* (25), 11119–11125.

(54) Atighilorestani, M.; Brolo, A. G. Comparing the Electrochemical Response of

Nanostructured Electrode Arrays. *Anal. Chem.* **2017**, *89* (11), 6129–6135.

For Table of Contents Use Only